Synthesis of nanoporous solid polymer electrolyte AuNiCe/NC hydrogenation membrane electrode

L. M. Duan[a], X. D. Li[a], Y. M. Shang[a], Y. H. Feng[b], H. H. Fan[a], S. Q. Wang[a], B. Yang[a,*]
[a]*Faculty of Materials Science and Engineering, Kunming University of Science and Technology, Kunming, Yunnan 650093, China*
[b]*Hengxing University, Qingdao, Shandong 266100, China*

In this study, using graphite fiber cloth as the support, gold-based solid polymer electrolyte (SPE) membrane electrodes were synthesized by high-vacuum ion beam sputtering, nitrogen doping of the support, combined electrochemical dealloying, and hot-pressing technology. The application of the SPE membrane electrode to couple hydrogen evolution and liquid organic hydrogen storage is of significant importance for sustainable hydrogen energy and efficient carbon dioxide conversion. Using various characterization techniques, we systematically analyzed the phase structure, surface morphology, porous structure, and electrocatalytic performance of the membrane electrode for the hydrogenation of cyclohexene. The results indicated that doping the carbonaceous support with nitrogen (NC), doping with cerium as catalyst promoter, and combined electrochemical dealloying can all enhance the activity of the catalyst. Cerium doping provides the catalyst with oxygen vacancies for accelerated electron transfer. After combined electrochemical dealloying, AuNiCe/NC formed a three-dimensional bicontinuous porous structure. The electrochemically active surface area increased by 23.94 times, the energy consumption of catalytic cyclohexene hydrogenation decreased by 35.7%, and current efficiency and the formation rate of cyclohexane increased by 54.9% and 29.4%, respectively.

(Received December 15, 2023; Accepted March 4, 2024)

Keywords: High-vacuum ion beam sputtering, Combined electrochemical dealloying, Nanoporous structure, Au-based SPE membrane electrode, Cyclohexene hydrogenation

1. Introduction

Hydrogenation of unsaturated organic compounds is one of the most important chemical transformations,[1] widely employed in the synthesis of pharmaceuticals,[2] functional materials,[3] and fine chemicals.[4] However, traditional thermocatalytic hydrogenation technologies are constrained by harsh reaction conditions such as high pressures and high temperatures.[5, 6] Therefore, electrocatalytic hydrogenation, which combines solid polymer electrolyte (SPE)-based hydrogen evolution technology with the hydrogenation of unsaturated organic compounds,[7] is an attractive alternative method.

Currently, the application of gold in hydrogenation reactions is limited, mainly because the hydrogen adsorption and activation capabilities of gold catalysts are lower than those of traditional metal catalysts based on metals like platinum, palladium, and nickel.[8, 9] However, gold-loaded catalysts exhibit unique hydrogenation selectivity.[10, 11] Modifying catalytic reactions by incorporating a second metal and utilizing the synergistic effect between gold and the second metal element adjusts the electronic structure of gold to enhance electrocatalytic activity.[12] Alternatively, the rare-earth element cerium can be doped into Au-M catalysts as a catalyst promoter, where the metal oxide CeO_x anchors gold nanoparticles, thereby enhancing stability and catalytic activity.[13]

* Corresponding author: yangbin@kust.edu.cn
https://doi.org/10.15251/DJNB.2024.191.369

Based on the effective catalysis of cobalt phthalocyanine in the reduction of oxygen,[14] carbon materials (such as carbon nanotubes, ordered mesoporous graphite arrays, graphene, and other carbon compounds) exhibited excellent catalytic activity after nitrogen doping.[15-17] When combined with platinum or non-platinum catalysts, such nitrogen-doped carbon materials demonstrated enhanced catalytic performance and stability.[18] During the electrochemical dealloying process of platinum-based catalysts, the use of different anionic acids has varying effects on the enhancement of the specific surface area (SSA) and electrochemically active surface area (ESA).[19, 20] For instance, hydrochloric acid (HCl) contributes to increasing the SSA of the catalyst, while perchloric acid ($HClO_4$) enhances the ESA by modifying the active sites of the catalyst.

In this study, nitrogen-doped graphite fiber cloth (NC) was used as a support in the preparation of nanoporous SPE-AuNiCe/NC hydrogenation membrane electrodes using high-vacuum ion beam sputtering (IBS) and combined electrochemical dealloying. Physicochemical characterization methods were employed to analyze the impact of using cerium as a promoter and a nitrogen-doped versus a pristine carbonaceous material as the support and the effect of the surface component structures on the catalytic performance of cyclohexene hydrogenation to enhance the composition-structure-activity relationship of gold-based catalysts.

2. Experimental section

Using pristine or nitrogen-doped graphite fiber cloth (C or NC) as supports, as well as gold, as the basic metal, nickel and cerium, as modifiers, Au/C, Au/NC, AuNi/NC (denoted as A-0), and AuNiCe/NC (denoted as B-0) catalysts were prepared at 210 °C using IBS technology. Combined dealloying treatment was applied to the B-0 catalyst by etching with a 0.25 mol L^{-1} HCl solution at 50 °C for 40 s and with a 0.15 mol L^{-1} $HClO_4$ solution at 60 °C for 90 min, yielding nanoporous dealloyed AuNiCe/NC catalyst (denoted as B-1).

The samples Au/C, Au/NC, A-0, B-0, and B-1 were individually immersed in a 5% Nafion solution, PTFE, and deionized water for 30 min. After natural air-drying, the samples were placed in a muffle furnace at 600 °C and heated for 60 s. The Nafion membranes were sequentially boiled for 60 min in a 5% hydrogen peroxide solution, a 0.5 mol L^{-1} sulfuric acid solution, and in deionized water, and then subjected to natural air-drying. Subsequently, the treated samples and Nafion membrane were hot-pressed at 175 °C for 180 s to synthesize SPE membrane electrodes. The synthesized SPE-Au/C, SPE-Au/NC, SPE-A-0, SPE-B-0, and SPE-B-1 membrane electrodes were placed between the cathode and anode chambers of the liquid-phase hydrogenation device.[21] A mixed solution of cyclohexene, glycerol, and PEG600 with a volume ratio of 3:1:1 was added to the cathode chamber (50 mL) at 50 °C, while the anode chamber (80 mL) was filled with a 0.5 mol L^{-1} sulfuric acid solution at room temperature. The anode chamber was externally connected to a direct current circuit with an electrolysis potential set at 1.6 V, while the cathode chamber was connected to an electrochemical workstation (CHI 440B, Shanghai, China). The hydrogenation potential was determined by cyclic voltammetry (CV) in the test range of -3.0 to 0 V (vs Ag/AgCl) with a scan rate of 50 mV s^{-1}. According to the Tafel curve fitting equation $\Delta E = a + blg|j|$ (where ΔE is the overpotential, a and b are Tafel constants, and j is the current density), the relationship between ΔE and $\lg|j|$ is linear. Extrapolating the Tafel line to intersect for $\Delta E = 0$ provides the exchange current density (j_0). Finally, a 60-min cyclohexene hydrogenation experiment was conducted under a constant hydrogenation potential using the bulk electrolytic coulombic (BEC) method.

The phase compositions of the catalysts were determined by X-ray diffraction (XRD, D/Max2200 with CuKα X-ray source). The surface morphology and micro-region crystal phases of the catalysts were characterized by high-resolution transmission electron microscopy (HRTEM) and scanning transmission electron microscopy coupled with energy dispersive X-ray spectroscopy (STEM-EDS) using a Tecnai G2 TF30 instrument. X-ray photoelectron spectroscopy (XPS, PHI5000 Versa Probe II X) was employed to characterize the surface atom distribution and ion valence states of the catalyst. Inductively coupled plasma optical emission spectroscopy (ICP-OES) was used to determine the contents and doping ratios of Au, Ni, and Ce in the samples.

A Brunauer-Emmett-Teller (BET) surface area analyzer (Quadrasorb SIBET) was used for multi-point isotherm nitrogen adsorption-desorption measurements to determine the pore size distributions and SSA of the samples. Gas chromatography-mass spectrometry (GC-MS) was employed to analyze the hydrogenation products of cyclohexene.

3. Results and discussion

3.1. Nitrogen doping of the carbonaceous support

The hydrogenation test results of SPE-Au/C and SPE-Au/NC using a liquid-phase hydrogenation device are shown in Figure 1(a) (CV curves) and Figure 1(b) (Tafel curves). The results of the electrochemical performance presented in Table 1 indicated that the peak potential $|E_d|$ (a smaller $|E_d|$ indicates lower energy consumption) of SPE-Au/NC shifted positively by 0.072 V compared to SPE-Au/C. Additionally, the hydrogenation peak area (S) increased by 58.6%, and the j_0 value improved by 11%. This enhancement was attributed to the nitrogen doping of the Au-based catalyst support, directly impacting the hydrogenation sensitivity of the membrane electrode and increasing the absolute rate of the oxygen reduction reaction.

Table 1. Electrochemical performance data of the samples SPE-Au/C and SPE-Au/NC.

Samples	S (mA V^{-1})	j_0 (mA cm^{-2})	$\|E_d\|$ (V)
SPE-Au/C	1.276×10^{-4}	2.111×10^{-3}	1.669
SPE-Au/NC	2.024×10^{-4}	2.343×10^{-3}	1.597

Figure 1(c) shows the XPS survey spectra of graphite fiber cloth and nitrogen-doped graphite fiber cloth, and the surface elemental compositions of C, O, and N for both supports are presented in Table 2. Pristine graphite fiber cloth also contained a certain amount of nitrogen on its surface, which increased by 675.97% after nitrogen doping. The deconvolution of the N 1s XPS spectra for both supports is illustrated in Figure 1(d). For the graphite fiber cloth surface, three peaks present at 399.08 eV, 400.17 eV, and 402.82 eV corresponded to pyridinic nitrogen (10.70 at%), graphitic nitrogen (71.39 at%), and N-oxide species (17.91 at%), respectively.[22]

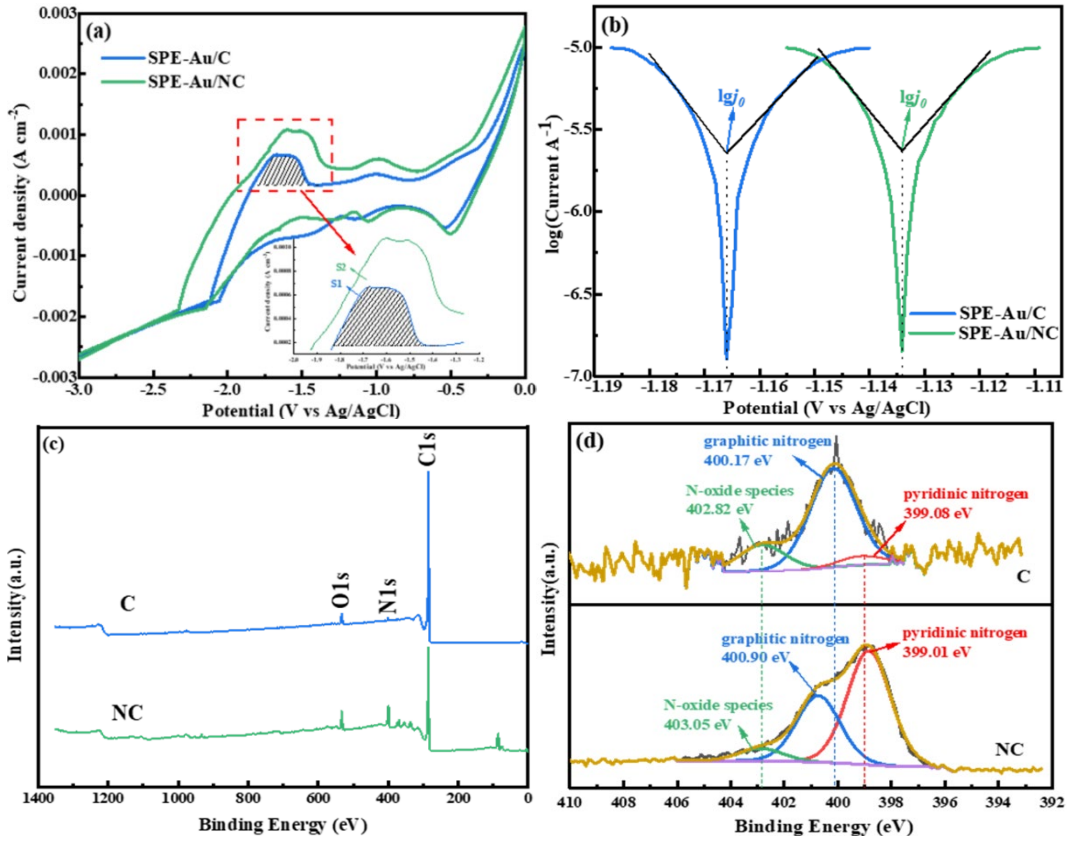

Fig. 1. (a) CV curves and (b) Tafel curves of the SPE-Au/C and SPE-Au/NC membrane electrodes; (c) full XPS spectra of graphite fiber cloth and nitrogen-doped graphite fiber cloth; (d) deconvoluted N 1s spectra.

Table 2. Elemental content on the surface of graphite fiber cloth and nitrogen-doped graphite fiber cloth.

Samples Number	Surface atomic content (at%)		
	C1s	N1s	O1s
C	94.49	1.79	3.72
NC	79.38	13.89	6.73

For the surface of the nitrogen-doped graphite fiber cloth, the three N 1s peaks were observed at 399.01 eV for pyridinic nitrogen (59.02 at%), 400.90 eV for graphitic nitrogen (34.45 at%), and 403.05 eV for N-oxide species (6.53 at%). The data indicated that nitrogen doping can selectively enhance the pyridinic nitrogen content on the support surface (increased by 451.6%). In acidic media, pyridinic nitrogen can promote the oxygen reduction activity in nitrogen-containing carbon compounds.[23-26] Therefore, the changes in the catalytic performance of SPE-Au/NC are related to the increased pyridinic nitrogen content, and further investigations were conducted with Au-based catalysts loaded on nitrogen-doped graphite fiber cloth.

3.2 XRD analysis

XRD patterns of the samples A-0, B-0, and B-1 are shown in Figure 2, and the ICP-OES results are presented in Table 3. Figure 2(a) indicated the presence of Au(200) and Au(311) crystal planes in A-0, B-0, and B-1 based on the diffraction peaks at 2θ angles of 44.38° and 77.56°. Additionally, B-1 exhibited peaks of the Au(111) and Au(220) crystal planes at 2θ angles of 38.6° and 65.0°. According to Figure 2(b), the diffraction peaks of Au(200) and Au(311) in B-0 shifted towards larger angles compared to A-0, and the greater values of the full width at half maximum suggested enhanced crystallinity and grain refinement in the membrane layer. The Au(200) and

Au(311) diffraction peaks of B-1 exhibited a more significant shift towards larger angles compared to B-0, and the diffraction peak intensity further increased. Additionally, diffraction peaks of Au(111) and Au(220) crystal planes were present, indicating that the exposed crystal plane status on the catalyst surface was altered to form an Au-rich surface, leading to lattice distortion[27] and a decrease in interplanar distance, which is conducive to enhancing the electron cloud density in the d-band of Au to promote electron conduction and enhance the catalytic activity of the catalyst.[28] No diffraction peaks of elemental Ni were observed in the samples, indicating the formation of a well-dispersed (Au) solid solution phase. Furthermore, no diffraction peaks of Ce were observed in B-0 and B-1, suggesting the possible formation of amorphous cerium oxide dispersed at grain boundaries or present in amounts below the detection limit.

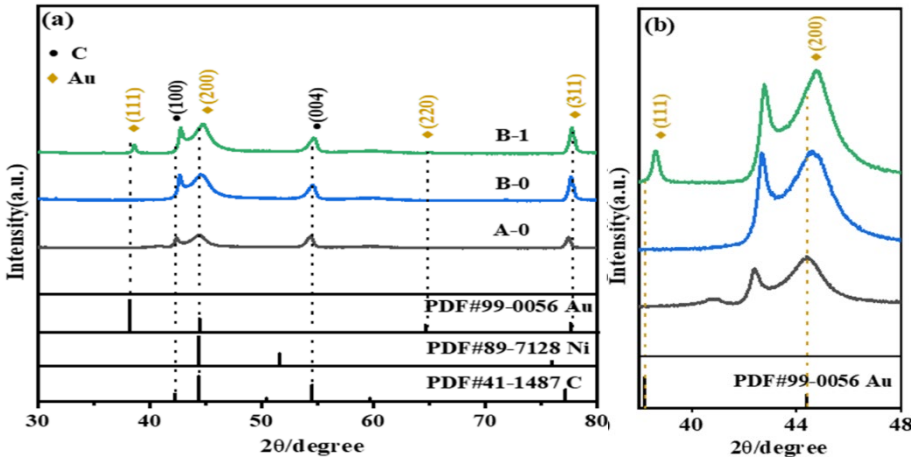

Fig. 2. (a) Overlaid XRD patterns of the samples A-0, B-0, and B-1; (b) local magnification of XRD patterns.

Table 3. ICP-OES results for A-0, B-0, and B-1.

Samples Number	Elemental content (at%)			Au : Ni
	Au	Ni	Ce	
A-0	72.58	27.42	-	1 : 0.38
B-0	60.35	33.04	6.21	1 : 0.55
B-1	97.36	0.95	1.69	1 : 0.01

3.3 STEM-EDS analysis

The STEM-EDS results for the samples A-0, B-0, and B-1 are shown in Figure 3. Figure 3(a, b) indicated the formation of a dense Au-Ni alloy catalyst with uniform distribution on the surface of A-0. According to Figure 3(c, d), a few porous structures were present on the surface of the B-0 membrane layer with a relatively uniform distribution of Au, Ni, and Ce elements. This morphology was attributed to the catalyst preparation under vacuum conditions, where the differences in the undercooling temperatures of Au, Ni, and Ce led to the preferential nucleation of Au and Ni, while the Ce atoms, with a larger atomic radius (0.27 nm) and the lowest melting point (795 °C), dispersed and deposited at grain boundaries. This distribution hinders the movement of grain boundaries and refines the grains, leading to the appearance of a small number of pores, which is conducive to the further dissolution of Ni during electrochemical dealloying, thereby increasing the SSA to provide more active sites.

Figure 3(e) shows the STEM image of B-1, revealing a three-dimensional bicontinuous porous structure on its membrane surface.[29]

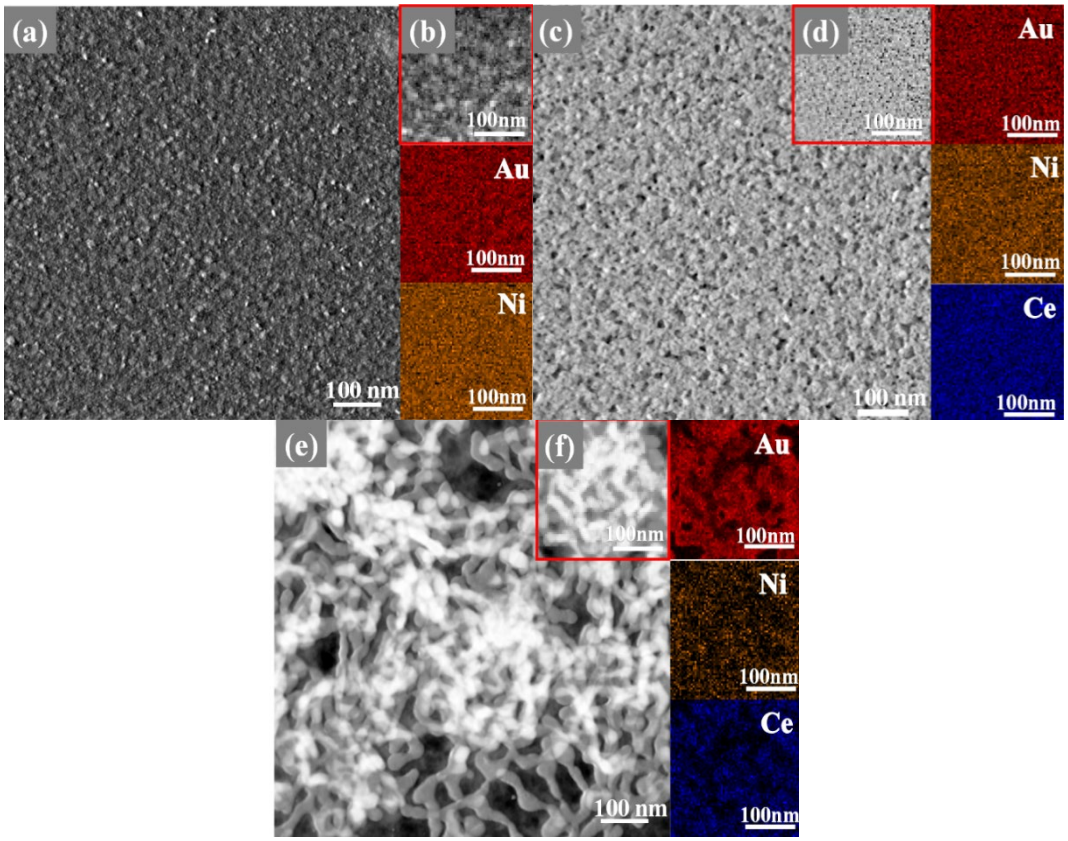

Fig. 3. STEM images and EDS maps of the samples A-0, B-0, and B-1. (a) (b) A-0; (c) (d) B-0; (e) (f) B-1.

Most of the particles were hyperbolic and had pores that formed at regions with negative curvature and were interconnected, while columnar particles formed at regions with positive curvature. This structure increased the SSA of the sample, providing more surface defects and numerous active sites, which can alter the local electronic structure to exhibit high catalytic activity for molecular adsorption. Figure 3(f) shows the EDS mapping of B-1, revealing that the particles were composed of Au, Ni, and Ce elements. The EDS mapping indicated a higher concentration of Au than Ni and Ce in the particles, indicating substantial etching of Ni and Ce in the catalyst, forming an Au-rich surface, which was consistent with the results in Table 3.

3.4. HRTEM analysis

The analysis results of the exposed crystal planes on the surfaces of the samples A-0, B-0, and B-1 are shown in Figure 4. The grains $A_{1\sim3}$, $B_{1\sim3}$, and $C_{1\sim3}$ were identified in the figure, and their crystal planes were calibrated using fast Fourier transform (FFT) to obtain the interplanar distance (*d* values).

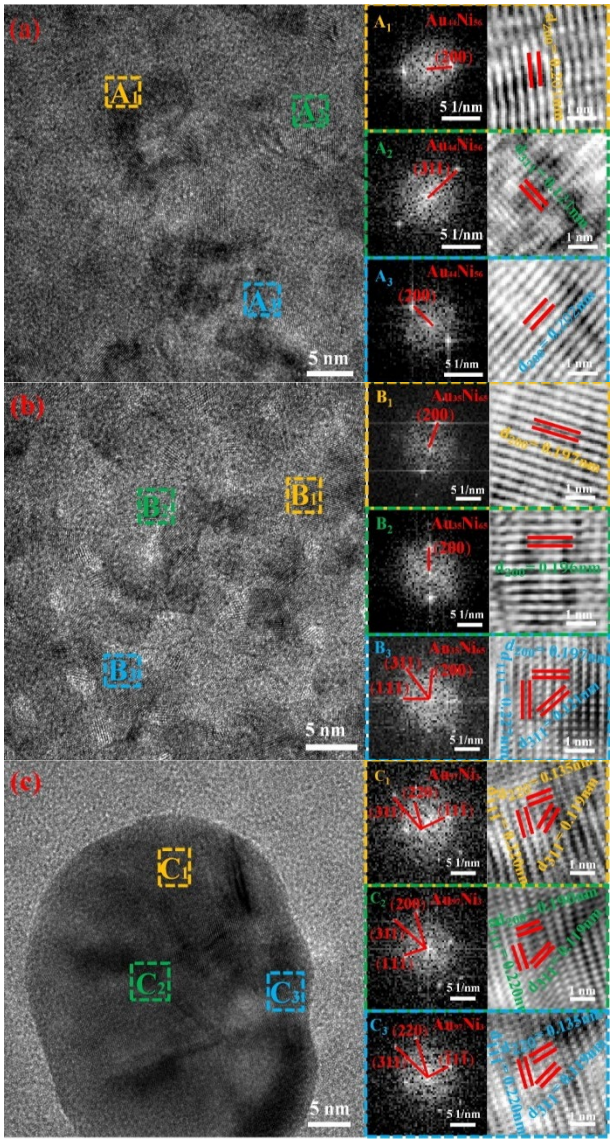

Fig. 4. HRTEM images of (a) A-0, (b) B-0, and(c) B-1. FFT and IFFF images of $A_{1\sim3}$, $B_{1\sim3}$, and $C_{1\sim3}$ corresponding to the marked areas in (a), (b), and (c).

According to Figure 4(a) and (b), the d values of Au(200) in A-0 and B-0 were 0.201 nm and 0.197 nm, respectively, while those of Au(311) were 0.123 nm and 0.121 nm, respectively. The *d* values of Au(200) and Au(311) in A-0 were close to the standard interplanar distance of pure Au (0.203 nm and 0.123 nm), while the corresponding *d* values for B-0 showed a slight decrease, possibly due to crystal plane contraction induced by Ce doping. Figure 4(c), the d values of Au(111), (220), (200), and (311) for B-1 were 0.220, 0.135, 0.190, and 0.119 nm, respectively, with a further decrease of 4% to 6% compared to the standard interplanar distances of pure Au, consistent with the shift towards larger angles in the XRD diffraction peaks. The smaller distances between the crystal planes are probably caused by the smaller atomic radius of Ni that entered the lattice of Au, resulting in lattice compression, while Ce atoms doped along the grain boundaries act as anchors, further reducing the interplanar distance. Additionally, the electrochemical dealloying process resulted in significant etching of Ni and Ce atoms on the surface of the AuNiCe catalyst, generating numerous zero-dimensional defects on the Au surface, causing lattice contraction.[30, 31] The contraction strain of Au is a crucial factor in enhancing the catalytic performance of AuNiCe/NC.[32]

3.5. XPS analysis

Figure 5 shows the electronic structure and chemical state spectra on the surfaces of A-0, B-0, and B-1. The full-scan spectra (0-1400 eV) in Figure 5(a) indicated the presence of Ni, O, C, and Au elements in A-0 and Ce, Ni, O, C, and Au elements in B-0. In B-1, after combined dealloying of B-0, the levels of Ni and Ce were below the detection limit, while the intensity of Au signal increased, consistent with the ICP results.

Figure 5(b) shows the deconvoluted Ni 2p XPS spectra of the A-0, B-0, and B-1 samples. For A-0, six Ni 2p peaks were observed (852.27, 855.74, 861.55, 869.57, 873.05, and 880.82 eV), which were identified as Ni^0, Ni^{2+}, and shake-up peaks.[33, 34] The proportions of Ni^0 and Ni^{2+} were 8.48 at% and 30.66 at%, respectively, indicating that the chemical state of Ni on the surface of A-0 was mainly Ni^{2+}, possibly due to oxidation by air.[35] The Ni 2p deconvolution results of B-0 were similar to those of A-0. The Ni 2p spectrum of B-1 was not further analyzed due to its lower Ni content.

Figure 5(c) shows the deconvoluted Ce 3d XPS spectra of B-0 and B-1. For B-0, the spectrum exhibited ten peaks, indicating the presence of Ce^{3+} and Ce^{4+} oxides. The coexistence of Ce^{3+} and Ce^{4+} as oxidation-reduction pairs easily generates oxygen vacancies within the lattice. These vacancies serve as electron transfer channels in the redox reactions of catalysts, enhancing electron transfer rates,[36] thereby improving catalytic activity. After combined dealloying of B-0, the Ce content in the obtained B-1 sample sharply decreased and was not further analyzed.

Figure 5(d) shows the Au $4f_{7/2}$ and Au4 $f_{5/2}$ spin-splitting peaks of Au for the samples A-0, B-0, and B-1, which were fitted with two peaks corresponding to the binding energy of elemental Au^0. The Au $4f_{7/2}$ binding energies were shifted to higher values by 0.08 eV, 0.17 eV, and 0.42 eV for A-0, B-0, and B-1, respectively, compared to pure Au (84.0 eV). A shift of the Au $4f_{7/2}$ peak is related to the catalytic activity of the catalyst, and a larger positive shift indicates higher catalytic activity.[37] This shift is likely influenced by the composition of the areas surrounding the Au elements, such as surface oxygen vacancies, forming the Au_n-O-Ni_m system,[38] which causes the Au $4f_{7/2}$ peak to shift towards higher binding energy.

Figure 5(e) shows the deconvolution results of the O 1s A-0, B-0, and B-1. In A-0, oxygen was mainly present as NiO, Ni-OH, and C=O formed by oxidation in air. In B-0 and B-1, oxygen mainly composed existed as lattice oxygen (O_L), adsorbed oxygen (O_{ads}), and surface adsorbed oxygen species (O^-). In For B-1, the O 1s peaks shift towards higher binding energies, and O_L disappeared due to the etching of cerium oxide, while the content of O_{ads} increased and surface O^- was transformed to O^{2-}, influenced by ClO_4^- in the etching solution.[39] This change in the environment around Au atoms caused the Au $4f_{7/2}$ peak shifts towards higher binding energies, thereby promoting the improvement in catalyst performance.

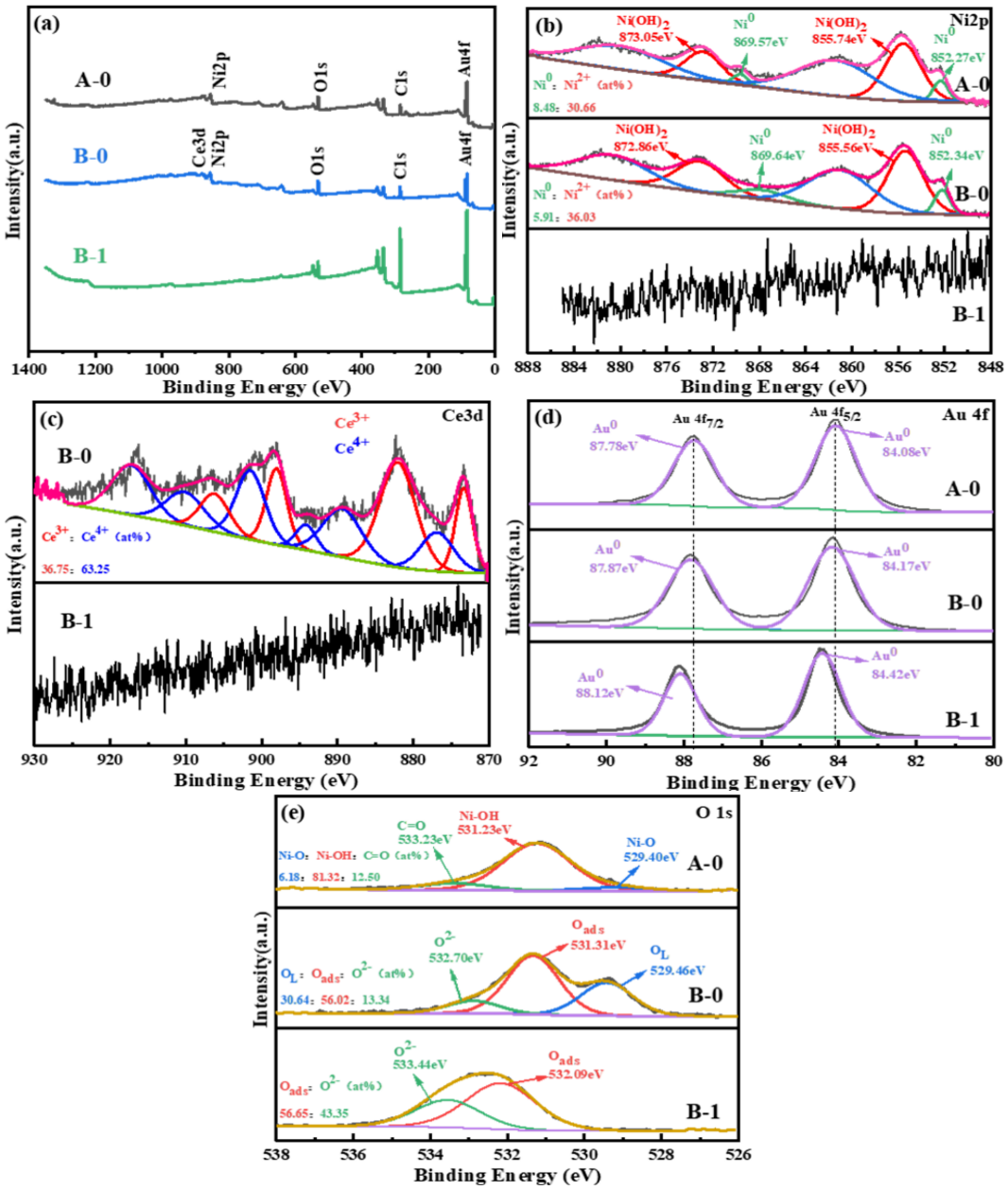

Fig. 5. Surface electronic structure and chemical state of A-0, B-0, and B-1.
(a) XPS survey spectra; deconvoluted (b) Ni 2p, (c) Ce 3d, (d) Au 4f, and (e) O 1s XPS spectra.

3.6. BET analysis

The surface pore structures of A-0, B-0, and B-1 were assessed using BET analysis, and the nitrogen adsorption-desorption isotherms and pore size distribution maps are shown in Figure 6. In Figure 6(a), A-0, B-0, and B-1 exhibited type IV adsorption isotherms within the relative pressure range, and A-0 and B-0 showed H4 hysteresis loops, while B-1 had an H3 hysteresis loop, indicating mesoporous and microporous characteristics.[40] The hysteresis loops for all three samples did not completely close. Combining the hysteresis loop types and the pore size distribution in Figure 6(b) suggested the presence of numerous micropores in the catalyst, causing incomplete nitrogen desorption and the loops not to close. The calculated SSAs of A-0, B-0, and B-1 were 2.69, 3.37, and 82.7 $m^2 g^{-1}$, respectively, showing a gradual increase, which is conducive to enhancing the adsorption capacity of the catalyst surface for cyclohexene, thereby improving the catalytic hydrogenation performance.[41]

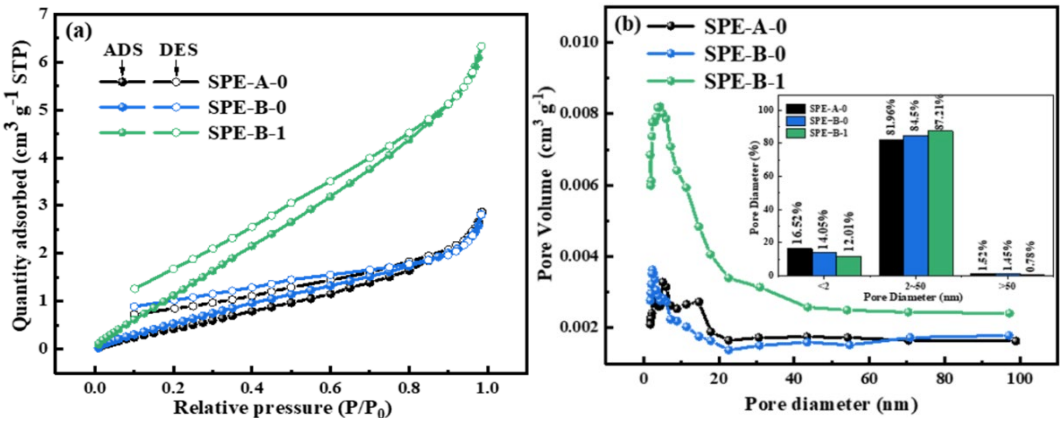

Fig. 6. (a) Nitrogen adsorption and desorption isothermal curves; (b) pore size distributions of A-0, B-0, and B-1.

3.7. Catalytic cyclohexene hydrogenation performance analysis

The ESA value represents the actual area of catalytically active sites in contact with the electrolyte, directly reflecting the quantity of active sites per unit surface area.[42] According to Equation (1), the ESA values of the samples can be calculated using the CV and ICP-OES results (see Table 3).

$$\mathrm{ESA} = \frac{s}{m \cdot v \cdot c} \tag{1}$$

where s is the area of the hydrogen desorption peak, m is the loading amount of Au on an electrode area of 1 cm^2, v is the scan rate, and c is the hydrogen adsorption capacitance of Au (0.424 mC cm^{-2}).

Table 4. ESA and SSA results for the samples SPE-A-0, SPE-B-0, and SPE-B-1.

Samples	SPE-A-0	SPE-B-0	SPE-B-1
ESA(m^2 g^{-1})	12.27	21.87	545.55
SSA(m^2 g^{-1})	2.69	3.37	82.7

Figure 7 shows the CV, Tafel, and BEC results obtained for the SPE membrane electrodes in the liquid-phase hydrogenation device connected to the CHI440B instrument. The CV curves of SPE-A-0, SPE-B-0, and SPE-B-1 in Figure 7(a) were obtained at a scan rate of 50 mV s^{-1}, and the ESA values calculated according to Equation (1) are summarized in Table 4, with values of 12.27, 21.87, and 545.55 m^2 g^{-1}, respectively. The ESA of SPE-B-0 increased by 78.2% compared to SPE-A-0, while that of SPE-B-1 exhibited an increase of 23.94 times compared to the ESA of SPE-B-0. Combining with the SSA results obtained from the BET analysis indicated that the number of catalytically active sites was related to the SSA of the samples. The combined electrochemical dealloying process significantly enhanced the ESA by increasing the SSA of the SPE electrode, thereby improving its catalytic performance.

The exchange current density j_0 of the SPE membrane electrode can be obtained from the Tafel curve in Figure 7(b), representing the absolute rate of oxidation-reduction reactions at the equilibrium potential. The calculations resulted in j_0 values of 2.071×10^{-3}, 2.516×10^{-3}, and 3.592×10^{-3} A·cm^{-2} for SPE-A-0, SPE-B-0, and SPE-B-1, respectively. The larger the j_0 value, the lower the potential required to achieve the same reaction rate, resulting in lower energy consumption. The observed trend was consistent with the trend of the hydrogenation potentials of SPE-A-0, SPE-B-0, and SPE-B-1 shown in the CV curves in Figure 7(a) (-1.65, -1.59, and -1.04 V, respectively).

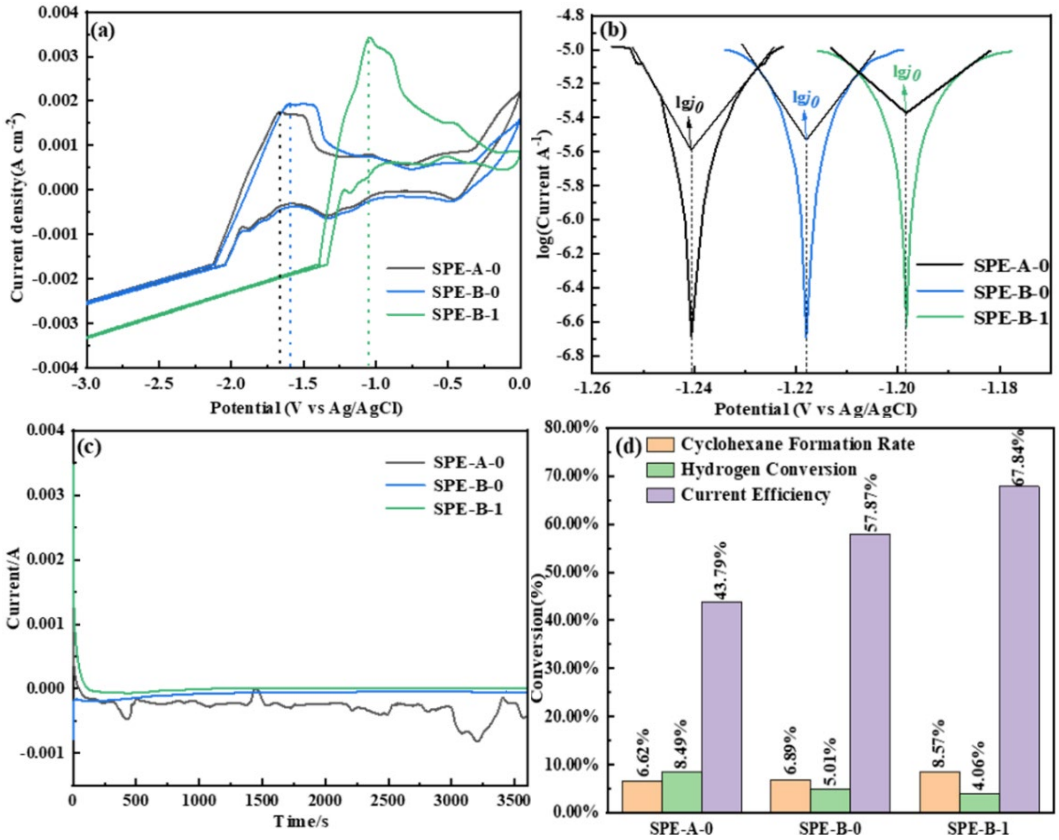

Fig. 7. Cyclohexene hydrogenation performance of SPE-A-0, SPE-B-0, and SPE-B-1; (a) CV curves; (b) Tafel curves; (c) BEC electrolytic curves; (d) cyclohexane formation rate, hydrogen conversion rate, and current efficiency.

Figure 7(c) reflects the BEC electrolysis curves of the cyclohexene hydrogenation process on the SPE membrane electrodes. The BEC curves of SPE-B-0 and SPE-B-1 entered a stable stage at around 250 s, while the BEC curve of SPE-A-0 showed the zigzagged line, possibly due to the slower hydrogenation on the surface of SPE-A-0, causing an imbalance between cyclohexene adsorption and cyclohexane desorption on the membrane electrode surface, which affects the stability of the hydrogenation reaction.

According to Equation (2) and the GC-MS results, the cyclohexane formation rate ($\omega_{C_6H_{12}}$), hydrogen conversion rate (ω_{H_2}), and cyclohexene hydrogenation current efficiency (η) were calculated, and the results are shown in Figure 7(d).

$$\eta = \frac{\omega_{C_6H_{12}}}{\omega_{C_6H_{12}} + \omega_{H_2}} \tag{2}$$

After electrocatalytic hydrogenation, the ω_{H_2} of SPE-A-0, SPE-B-0, and SPE-B-1 were determined as 8.49%, 5.01%, and 4.06%, respectively; the $\omega_{C_6H_{12}}$ values were 6.62%, 6.89%, and 8.57%, and the corresponding η values were calculated as 43.79%, 57.87%, and 67.84%. The gradual decrease in ω_{H_2} of SPE-A-0, SPE-B-0, and SPE-B-1 indicated that Ce doping and combined electrochemical dealloying can partially inhibit the hydrogen evolution side reaction during cyclohexene hydrogenation. The $\omega_{C_6H_{12}}$ of SPE-B-1 was significantly higher than that of SPE-A-0 and SPE-B-0, which was attributed to the increase in SSA due to the combined electrochemical dealloying treatment, promoting the diffusion of cyclohexene on the membrane electrode surface and significantly increasing the number of active sites on the surface, thereby resulting in excellent cyclohexene hydrogenation conversion and current efficiency.

4. Conclusions

In this study, Au-based catalysts were prepared on carbonaceous supports using high vacuum IBS, nitrogen doping of the support, and combined electrochemical dealloying. The materials were then used to synthesize the membrane electrodes SPE-A-0, SPE-B-0, and SPE-B-1 by hot pressing technology, which were subsequently utilized in the coupled process of hydrogen evolution and liquid organic hydrogen storage. The analysis results indicated that nitrogen doping of the carbonaceous support can promote oxygen reduction activity in nitrogen-containing carbon compounds (the surface pyridinic nitrogen content increased by 451.6%), increasing the concentration of oxygen vacancies to enhance electron transfer efficiency. The surface of the dealloyed catalyst surface exhibited a three-dimensional bicontinuous nanoporous structure with a high SSA value of 82.7 m^2 g^{-1}. The majority of the particles in these structures were hyperbolic, and a large number of zero-dimensional defects contributed to the lattice contraction of Au. The binding energy of Au^0 in the Au $4f_{7/2}$ XPS spectrum of the surface of the membrane electrode was higher than that of pure Au. Ni was mainly present as Ni^{2+}, and Ce existed in the form of Ce^{3+} and Ce^{4+} oxides. The content of O_{ads} increased, and O^- was transformed into O^{2-} due to the influence of ClO_4^- in the acidic solution. The ESA value of SPE-B-1 increased by 23.94 times compared to SPE-B-0, and the energy consumption for the catalytic cyclohexene hydrogenation was reduced by 35.7%, while the current efficiency of cyclohexene hydrogenation and the formation rate of cyclohexane increased by 54.9% and 29.4%, respectively. These results demonstrate the membrane's excellent low-temperature catalytic hydrogenation activity and the ability to inhibit hydrogen evolution side reactions.

Acknowledgements

This work was supported by the National Natural Science Foundation of China (52361031, 51861017).

References

[1] J. J. Yang, H. Y. Qin, K. Yan, et al., Advanced Synthesis & Catalysis, 363(24), 5407(2021); https://doi.org/10.1002/adsc.202101249

[2] J. D. Hayler, D. K. Leahy, E. M. Simmons, Organometallics, 38(1), 36(2018); https://doi.org/10.1021/acs.organomet.8b00566

[3] P. J. Chirik, Acc. Chem. Res, 48(6), 1687(2015); https://doi.org/10.1021/acs.accounts.5b00134

[4] C. Yang, S. Bai, Y. Feng, et al., ChemCatChem, 11(9), 2265(2019); https://doi.org/10.1002/cctc.201900232

[5] A. Mori, Y. Miyakawa, E. Ohashi, et al., Organic Letters, 8(15), 3279(2006); https://doi.org/10.1021/ol061147j

[6] J. S. Reddy, B.-H. Xu, T. Mahdi, et al., Organometallics, 31(15), 5638(2012); https://doi.org/10.1021/om3006068

[7] N. Itoh, W. Xu, S. Hara, et al., Catalysis today, 56(1), 307(2000); https://doi.org/10.1016/S0920-5861(99)00288-6

[8] Y. X. Ma, Z. Su, N. F. Tang, et al., Chemical Physics Letters, 775, 138604(2021); https://doi.org/10.1016/j.cplett.2021.138604

[9] T. Zheng, F. S. Wu, H. Fu, et al., Chemistry-An Asian Journal, 16(16), 2298(2021);

https://doi.org/10.1002/asia.202100472

[10] G. Li, C. Zeng, R. Jin, JACS, 136(9), 3673(2014); https://doi.org/10.1021/ja500121v

[11] J. Lin, H. Abroshan, C. Liu, et al., J. Catal, 330(354(2015); https://doi.org/10.1016/j.jcat.2015.07.020

[12] H. S. Wei, X. Wei, X. F. Yang, et al., Chinese Journal of Catalysis, 36(2), 160(2015); https://doi.org/10.1016/S1872-2067(14)60254-0

[13] J. Q. Ye, M. Z. Jing, Y. Liang, et al., Nanoscale Horizons, 8(6), 812(2023); https://doi.org/10.1039/D3NH00103B

[14] R. Jasinski, Nature, 201(4925), 1212(1964); https://doi.org/10.1038/2011212a0

[15] L. Chen, Z. Chen, Z. Huang, et al., J. Phys. Chem. C, 119(52), 28757(2015); https://doi.org/10.1021/acs.jpcc.5b10246

[16] I.-H. Lin, Y.-H. Lu, H.-T. Chen, PCCP, 18(17), 12093(2016); https://doi.org/10.1039/C6CP00162A

[17] D. D. Liu, J. X. Zhang, C. Zhang, et al., J Porous Mat, 25(3), 913(2018); https://doi.org/10.1007/s10934-017-0503-1

[18] L. Jian-Feng, S. Ge, W. Ting, et al., Pol J Chem Technol, 24(3), 29(2022); https://doi.org/10.2478/pjct-2022-0019

[19] Y. H. Feng, B. Yang, J. X. Cai, et al., J Mater Eng Perform, 32(21), 9787(2023); https://doi.org/10.1007/s11665-023-07832-6

[20] X. D. Li, B. Yang, J. X. Cai, et al., J Solid State Electr, 27(10), 2799(2023); https://doi.org/10.1007/s10008-023-05580-0

[21] B. Y, J. G, D.H. Y (2018) An energy storage device for cyclic hydro-genation of unsaturated organic compounds (ZL201810342964.2)

[22] Y. Cao, S. Mao, M. Li, et al., Acs Catalysis, 7(12), 8090(2017); https://doi.org/10.1021/acscatal.7b02335

[23] L. M. Cao, Z. P. Lin, J. Huang, et al., Int J Hydrogen Energ, 42(2), 876(2017); https://doi.org/10.1016/j.ijhydene.2016.11.108

[24] D. Guo, R. Shibuya, C. Akiba, et al., Science, 351(6271), 361(2016); https://doi.org/10.1126/science.aad0832

[25] H. A. B. M. D. Weththasinha, Z. Yan, L. Gao, et al., Int J Hydrogen Energ, 42(32), 20560(2017); https://doi.org/10.1016/j.ijhydene.2017.06.011

[26] G. Wu, A. Santandreu, W. Kellogg, et al., Nano Energy, 29(83(2016); https://doi.org/10.1016/j.nanoen.2015.12.032

[27] T. Zhang, Y. Bai, Y. Q. Sun, et al., J. Mater. Chem. A., 6(28), 13735(2018); https://doi.org/10.1039/C8TA04087G

[28] H. M. Duan, Q. Hao, C. X. Xu, Journal of Power Sources, 280(483(2015); https://doi.org/10.1016/j.jpowsour.2015.01.136

[29] Q. Zheng, Y. Tian, X. Shen, et al., Appl. Phys. Lett., 119(6), 063101(2021).

[30] C. Chen, Y. Kang, Z. Huo, et al., Science, 343(6177), 1339(2014); https://doi.org/10.1126/science.1249061

[31] H.-L. Liu, F. Nosheen, X. Wang, Chem Soc Rev, 44(10), 3056(2015); https://doi.org/10.1039/C4CS00478G

[32] L. Gan, C. H. Cui, S. Rudi, et al., Topics in Catalysis, 57(1-4), 236(2013); https://doi.org/10.1007/s11244-013-0178-z

[33] L. J. Liu, H. Lou, M. Chen, Int J Hydrogen Energ, 41(33), 14721(2016); https://doi.org/10.1016/j.ijhydene.2016.05.188

[34] B. Q. Xia, N. Cao, H. M. Dai, et al., ChemCatChem, 6(9), 2549(2014); https://doi.org/10.1002/cctc.201402353

[35] G. Q. Liu, X. Zhang, C. J. Zhao, et al., New J Chem, 42(8), 6381(2018); https://doi.org/10.1039/C8NJ00446C

[36] D. R. Mullins, Surf Sci Rep, 70(1), 42(2015); https://doi.org/10.1016/j.surfrep.2014.12.001

[37] A. Naumkin, A. Y. Vasil'kov, Russ Chem B+, 62(2559(2013); https://doi.org/10.1007/s11172-013-0373-x

[38] G. K. Wertheim, S. B. Dicenzo, S. E. Youngquist, Physical Review Letters, 51(25), 2310(1983); https://doi.org/10.1103/PhysRevLett.51.2310

[39] Liang Huang, Xue Ping Zhang, Yu Jie Han, et al., Chem. Mater., 29(10), 4557(2017); https://doi.org/10.1021/acs.chemmater.7b01282

[40] R. Bardestani, G. S. Patience, S. Kaliaguine, Can J Chem Eng, 97(11), 2781(2019); https://doi.org/10.1002/cjce.23632

[41] B. Yang, L. D. Fang, L. H. Zan, et al., Int J Hydrogen Energ, 47(4), 2500(2022); https://doi.org/10.1016/j.ijhydene.2021.10.179

[42] D. Voiry, M. Chhowalla, Y. Gogotsi, N. A. Kotov, Y. Li, R. M. Penner, R. E. Schaak, P. S. Weiss, ACS Nano, 12(10), 9635(2018); https://doi.org/10.1021/acsnano.8b07700